Effect of myofibril architecture on the active contraction of dystrophic muscle. A mathematical model

Marco Stefanati[a], Yvan Torrente[b], José Félix Rodriguez Matas[a]

[a] *Department of Chemistry, Materials and Chemical Engineering "Giulio Natta", Politecnico di Milano, Piazza Leonardo da Vinci, 20133 Milan, Italy*
[b] *Stem Cell Laboratory, Department of Pathophysiology and Transplantation, Università degli Studi di Milano, Fondazione IRCCS Ca' Granda Ospedale Maggiore Policlinico, Milan, Italy*

Abstract

Duchenne muscular dystrophy (DMD) is a muscle degenerative disease caused by a mutation in the dystrophin gene. The lack of dystrophin leads to persistent inflammation, degeneration/regeneration cycles of muscle fibers, Ca^{2+} dysregulation, incompletely regenerated fibers, necrosis, fibrotic tissue replacement, and alterations in the fiber ultrastructure i.e., myofibril misalignment and branched fibers. This work aims to develop a comprehensive chemo-mechanical model of muscle-skeletal tissue accounting for dispersion in myofibrillar orientations, in addition to the disorders in sarcomere pattern and the fiber branching. The model results confirm a significant correlation between the myofibrillar dispersion and the reduction of isometric force in the dystrophic muscle and indicate that the reduction of contraction velocity in the dystrophic muscle seems to be associated with the local disorders in the sarcomere patterns of the myofibrils. Also, the implemented model can predict the force-velocity response to both concentric and eccentric loading. The resulting model represents an original approach to account for defects in the muscle ultrastructure caused by pathologies as DMD.

Keywords:
Skeletal muscle model, Fibril misalignment effect, Dystrophic skeletal muscle model

1. Introduction

Duchenne muscular dystrophy (DMD) is a common inherited muscle degenerative disease caused by a mutation in the dystrophin gene. The pathophysiology of the dystrophin deficiency in DMD muscle underlying the progressive weakness remains still an open question. Dystrophin provides mechanical stability to the sarcolemma but is also related to Ca^{2+} ion channel function (Petrof et al., 1993; Friedrich et al., 2008). As a consequence, the lack of dystrophin triggers persistent inflammation, degeneration/regeneration cycles of muscle fibers, and Ca^{2+} dysregulation. This set of events comprises the driving force for muscle degeneration, necrosis and fibrotic tissue replacement (Messina et al., 2006; Acharyya et al., 2007).

Studies in mdx mice, an animal model that reflects some of the human pathologies associated with DMD, show that the altered function of ion channels and the calcium overload in muscle fibers trigger cell damage pathways. This increases the frequency of degeneration/regeneration cycles leading to incompletely regenerated fibers, and gross alterations in the fiber ultrastructure i.e., morphologically abnormal, deformed and branched fibers (Friedrich et al., 2010; Buttgereit et al., 2013). These structural alterations steadily increase with age in the mdx mice after dystrophic onset as shown in Head et al. (1992). In contrast, in vitro motility assays of single mdx fiber myosin extracted by Friedrich et al. (2010) demonstrated unaltered

sliding velocities. In other words, motor protein function is preserved in dystrophic skeletal muscle. Therefore, it is expected that structural changes occurring during the course of the disease be associated with progressive muscle weakness.

Developments in nonlinear second harmonic generation (SHG) techniques have allowed characterizing how the dystrophic process affects myofibril arrangement and sarcomere geometry. Garbe et al. (2012) used a combined SHG microscopy together with tensor-based image processing to quantify morphological changes in the mdx mouse with age. They characterized fiber morphology at the myofibril and sarcomere scales. Two structural signatures were used, namely: the cosine angle of sum (CAS) that quantifies myofibrillar alignment, and the "Verniers" density (VD) that refers to local disruptions of the regular sarcomere lattice. They reported the appearance of fiber branching and morphological alterations throughout the course of the disease in mdx mice. In a posterior study by the same group, Buttgereit et al. (2013) showed morphological alterations to be a landmark for the onset and progression of the disease in the mdx mouse. They demonstrated the increase of fiber branching together with an increment in myofibril misalignment with age in dystrophic muscle. However, more interestingly, they report the presence of "chaotic" fibers with abnormal sarcomere arrangement (larger vernier density) and relative myofibrillar misalignment, with respect to the healthy case, even at a younger age where unbranched fibers still predominate. This suggests that branched fibers may develop from the chaotic fiber type. In addition, they also observed a significant reduction in CAS with age suggesting that CAS may explain, at least in part, muscle weakness in mdx fibers. This

aspect has been demonstrated by Schneidereit et al. (2018) by studying how alterations in the fiber ultrastructure affect single muscle fiber force production. Using a biomechatronic system combined with SHG microscopy they found a significantly reduced specific force in the mdx mouse as compared to the healthy subject. This reduction in specific force was directly correlated with a reduced Ca^{2+} sensitivity, and lower CAS and higher VD values in the dystrophic muscle, consistent with an abnormal fiber ultrastructure. They also reported an increase in myofibrillar disorder during concentric contraction.

Modern mathematical models of healthy and dystrophic muscle simulate the dynamic behavior of the tissue by coupling cross-bridge kinetics with cross-bridge distortion responsible for the active force generation (Heidlauf and Röhrle, 2014; Karami et al., 2019; Stefanati et al., 2020). However, most mathematical models consider neither myofiber misalignment nor fiber branching in their formulation. In other words, most models of skeletal muscle assume perfectly aligned myofibrils and perfect sarcomere lattice. The aim of this work is to develop a comprehensive chemo-mechanical model of muscle-skeletal tissue accounting for dispersion in myofibril orientations, in addition to the effect of fiber branching, in order to simulate the effect that changes in the muscle ultrastructure have on muscle weakness i.e., reduction in isometric force and contraction velocity. This model presents an evolution of our previously developed model (Stefanati et al., 2020) by explicitly introducing a more detailed description of the muscular fiber ultrastructure by incorporating the distribution of myofibril orientation in the model formulation. The resulting model represents an original approach to account for micromechan-

ical deffects i.e., myofibril misalignment associated with the DMD pathogenesis as eported by Schneidereit et al. (2018) and Buttgereit et al. (2013) on the dystrophic fiber. We assume, however, that the myosin function is not affected by the dystrophin lack (Friedrich et al., 2010). The manuscript is organized as follows, Section 2 elaborates on the modifications performed to the model of skeletal muscle proposed by Stefanati et al. (2020) to account for myofibril misalignment. This section also describes the specialization of the model to the one-dimensional case and the parameter identification procedure. Section 3 describes the main results obtained with the model and the comparison with experimental data reported in the literature. Finally, Section 4 presents some discussion and concluding remarks.

2. Methods

2.1. Mechanical model

The proposed model of skeletal muscle departs from the recent work by Stefanati et al. (2020) where the chemo-mechanical representation of the model is composed of two parts: (i) the myofilament Ca^{2+} kinetics and cross-bridge force generation (see Appendix A), and (ii) the mechanical model of the muscle composed of the active response of the fiber and the passive response of ECM (see Fig. 1a).

The mechanical characterization of the muscle is represented as a passive elastic element associated with the extracellular matrix (ECM) in parallel with an active element (fiber) composed of two elements: i) the myofibrils consisting on an active contractile element (myotubes) in series with an

elastic element, and ii) another elastic element in parallel with myofibril associated with the passive response of the muscle fiber (see Fig. 1a).

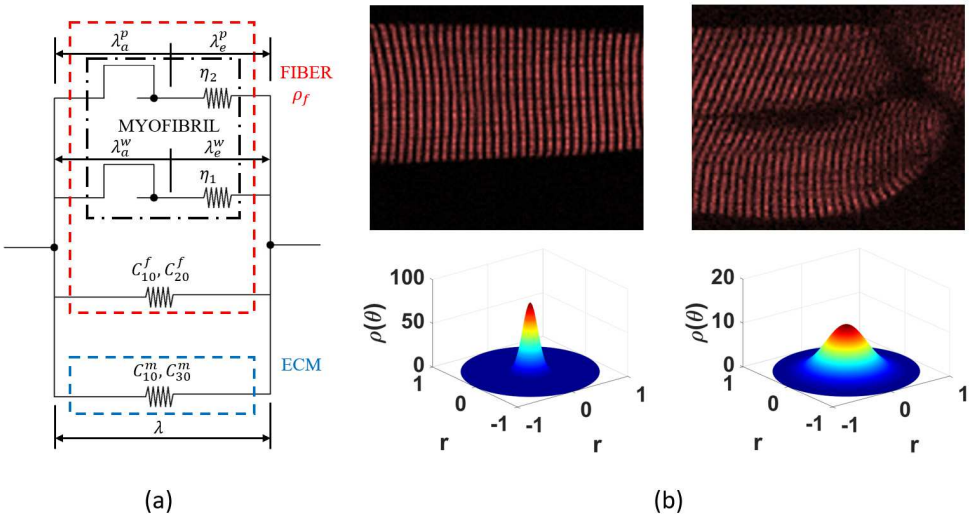

Figure 1: a) Mechanical representation of the muscle. The mechanical model is composed of a contractile element describing the myofibril response and a passive element describing the ECM elastic response. b, top-left) Myofibril organization in the healthy condition (adapted from Schneidereit et al. (2018)). b, bottom-left) Orientation distribution function in the C57Bl case (for b=20). b, top-right) Myofibril organization in the dystrophic condition (adapted from Schneidereit et al. (2018)). b, bottom-right) Orientation distribution function in the mdx case (for b=3).

Following Stefanati et al. (2020), we postulate the existence of a strain energy function (SEF) decoupled into volumetric and volume-preserving parts from which the stresses can be derived. In order to account for the active contraction of the skeletal muscle, the SEF is also a function of the active

stretches λ_a^w (pre-power stroke state) and λ_a^p (post-power stroke state),

$$W(\mathbf{C}, \mathbf{n}_0, \lambda_a^w, \lambda_a^p) = U(J) + \bar{W}(\bar{\mathbf{C}}, \mathbf{n}_0, \lambda_a^w, \lambda_a^p), \tag{1}$$

where $\mathbf{C} = \mathbf{F}^T\mathbf{F}$ is the right Cauchy-Green deformation tensor, with $\mathbf{F}$ the deformation gradient, $J = \det \mathbf{F}$ is the Jacobian, $\bar{\mathbf{C}} = J^{-2/3}\mathbf{C}$ is the modified right Cauchy-Green deformation tensor, and $\mathbf{n}_0$ is the so called preferred direction coincident with the muscle fiber orientation. The definition of λ_a^w and λ_a^p is found in Appendix A.

Following the classical approach used in modeling anisotropic soft tissues, the deviatoric part of the strain energy function is decoupled into a strain energy function related to the matrix and a strain energy function related to fibrous part,

$$\bar{W}\big(\bar{\mathbf{C}}, \mathbf{n}_0, \lambda_a^w, \lambda_a^p\big) = \bar{W}_{matrix}\big(\bar{\mathbf{C}}\big) + \rho_f \cdot \bar{W}_f\big(\bar{\mathbf{C}}, \mathbf{n}_0, \lambda_a^w, \lambda_a^p\big), \tag{2}$$

where ρ_f is the cross-section area fiber density (CSA fiber density) defined as the ratio between the total fiber area A_f and muscle area A_{musc} ($\rho_f \leq 1$).

Differently to Stefanati et al. (2020) where the myofibrils are assumed to be perfectly aligned and coincident with the direction of the muscle fiber, $\mathbf{n}_0$, in the present model this condition is relaxed by allowing the myofibrils to be distributed with a certain dispersion with respect to $\mathbf{n}_0$. Figure 1b, top panels, shows the myofibril arrangement for the healthy and the dystrophic mouse respectively, where myofibril misalignment is clearly noticeable in the dystrophic case. Figure 1b, bottom panels, shows the corresponding myofibril orientation distributions (definition of the von Mises distribution given at the end of this section).

To define the fiber dispersion, we assume the existence of a uniaxial myofibril orientation distribution function (ODF) $\rho(\mathbf{r}, \mathbf{n}_0) = \rho(-\mathbf{r}, \mathbf{n}_0)$ for $\mathbf{r}$ a referential unit vector (Gasser et al., 2006; Alastrué et al., 2009). Hence, the strain energy related to the fibers is defined as

$$\bar{W}_f\left(\bar{\mathbf{C}}, \mathbf{n}_0\right) = \frac{1}{4\pi} \int_{\mathbb{U}^2} \rho(\mathbf{r}, \mathbf{n}_0) \bar{W}_{mf}\left(\bar{\mathbf{C}}, \mathbf{r}, \lambda_a^{w,r}, \lambda_a^{p,r}\right) dA, \tag{3}$$

where $\bar{W}_{mf}(\bar{\mathbf{C}}, \mathbf{r}, \lambda_a^{w,r}, \lambda_a^{p,r})$ is the strain energy of the single myofibril with orientation $\mathbf{r}$, and $\lambda_a^{w,r}$, $\lambda_a^{p,r}$ the corresponding active stretches. In Equation 3, $\mathbb{U}^2$ stands for the unit sphere, the domain of integration of the ODF (see Figure 2).

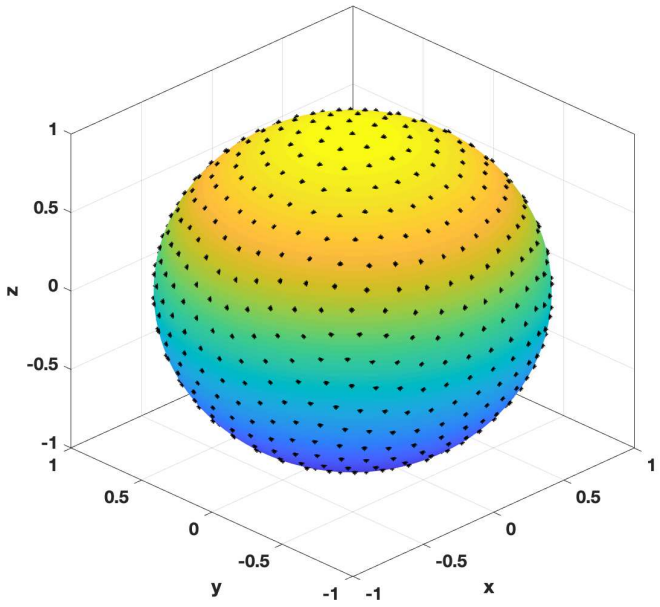

Figure 2: The unite sphere, $\mathbb{U}^2$, the domain of integration of the continuous orientation distribution function (ODF).

Also, the strain energy function of the myofibril is divided into a passive contribution and an active contribution associated with the muscular actin-myosin system,

$$\bar{W}_{mf}\left(\bar{\mathbf{C}},\mathbf{r},\lambda_a^{w,r},\lambda_a^{p,r}\right)=\bar{W}_{mf,p}\big(\bar{\mathbf{C}},\mathbf{r}\big)+\bar{W}_{mf,a}\left(\bar{\mathbf{C}},\mathbf{r},\lambda_a^{w,r},\lambda_a^{p,r}\right). \tag{4}$$

In order to guarantee frame invariance, the SEF is expressed in terms of the three principal invariants of $\bar{\mathbf{C}}$, and the quasi-invariants associated with the preferred direction $\mathbf{r}$

$$\begin{aligned} \bar{I}_1=\mathrm{tr}\bar{\mathbf{C}}, \qquad & \bar{I}_2=\frac{1}{2}[(\mathrm{tr}\bar{\mathbf{C}})^2-\mathrm{tr}\bar{\mathbf{C}}^2], \\ \bar{I}_3=\det\bar{\mathbf{C}}=1, \qquad & \bar{I}_4^r=\mathbf{r}\cdot(\bar{\mathbf{C}}\cdot\mathbf{r})=\lambda_r^2. \end{aligned} \tag{5}$$

Hence,

$$\bar{W}_{matrix}(\bar{\mathbf{C}}) = \bar{W}_{matrix}(\bar{I}_1,\bar{I}_2), \tag{6}$$

$$\bar{W}_{mf,p}(\bar{\mathbf{C}},\mathbf{r}) = \bar{W}_{mf,p}(\bar{I}_1,\bar{I}_2,\bar{I}_4^r), \tag{7}$$

$$\bar{W}_{mf,a}(\bar{\mathbf{C}},\mathbf{r},\lambda_a^w,\lambda_a^p) = \bar{W}_{mf,a}(\bar{I}_4^r,\lambda_a^{w,r},\lambda_a^{p,r}). \tag{8}$$

With the strain energy function so defined, it is possible to derive the first Piola-Kirchhoff stress tensor as,

$$\mathbf{P}=2\mathbf{F}\frac{\partial W}{\partial\mathbf{C}}. \tag{9}$$

We have assumed the matrix to be isotropic, whereas the myofibers are assumed intrinsically anisotropic (even though they behave as one-dimensional elements). The active behavior of the single myofibrils, $\bar{W}_{mf,a}$, is assumed as in Stefanati et al. (2020) i.e., as the sum of the contribution of the two states

of attached XBs: A_1 (attached pre-power stroke state) and A_2 (attached post-power stroke state),

$$\bar{W}_{mf,a}\left(\bar{I}_4^r, \lambda_a^{w,r}, \lambda_a^{p,r}\right) = \frac{1}{2}\eta_1 A_1 \left[\frac{1}{2}\ln(\bar{I}_4^r) - \ln\left(\lambda_a^{w,r}\right)\right]^2 + \\ + \frac{1}{2}\eta_2 A_2 \left[\frac{1}{2}\ln(\bar{I}_4^r) - \ln\left(\lambda_a^{p,r}\right)\right]^2, \tag{10}$$

where η_1 and η_2 are elastic constants for the pre- and post- power stroke dependent on the sarcomere lattice arrangement. The equations defining A_1 and A_2 are found in Appendix A.

Note that, even though the myofibrils are intrinsically anisotropic, the degree of fiber anisotropy depends on the characteristics of the ODF. In this work, we assume a transversely isotropic and π-periodic von Mises distribution (see Figure 1b, bottom panels)

$$\rho(\theta) = 4\sqrt{\frac{b}{2\pi}}\frac{\exp(b[\cos(2\theta)+1])}{\operatorname{erfi}(\sqrt{2b})}, \tag{11}$$

where $\cos(\theta) = \mathbf{r}\cdot\mathbf{n}_0$, and the positive concentration parameter b constitutes a measure of the anisotropy degree i.e., $b \to \infty$ implies transversely orthotropic, and $\operatorname{erfi}(x) = -i\operatorname{erf}(x)$ denotes the imaginary error function (Gasser et al., 2006).

2.2. Discretization on the microsphere

In order to render Eq. 3 operative, the integral on the unit sphere is expressed as

$$\bar{W}_f = \sum_{i=1}^{m} w^i \; \rho\left(\mathbf{r}^i, \mathbf{n}_0\right) \; \bar{W}_{mf}^i = \sum_{i=1}^{m} w^i \; \rho\left(\theta^i\right) \; \bar{W}_{mf}^i, \tag{12}$$

where $\theta^i = \cos^{-1}(\mathbf{r}^i \cdot \mathbf{n}_0)$ is the angle of the ith myofibril with respect to $\mathbf{n}_0$, and w^i a weighting factor. The discretisation of the continuous orientation distribution on the unit sphere $\mathbb{U}^2$ is obtained by means of m discrete orientation vectors $\{\mathbf{r}^i\}_{i=1,\dots,m}$ and weighting factors,$\{w^i\}_{i=1,\dots,m}$ satisfying

$$\frac{1}{4\pi}\int_{\mathbb{U}^2} \rho(\theta)\, \mathrm{d}A \approx \sum_{i=1}^{m} w^i\, \rho\left(\theta^i\right) = 1, \tag{13}$$

together with the constraints $\langle \mathbf{r} \rangle \approx \sum_{i=1}^{m} w^i\ \mathbf{r}^i = 0$ as well as $\langle \mathbf{r} \otimes \mathbf{r} \rangle \approx \sum_{i=1}^{m} w^i\ \mathbf{r}^i \otimes \mathbf{r}^i = \frac{1}{3}\mathbf{I}$.

In our model of the fiber, we use a discretization based on 632 directions obtained using the efficient spherical t-design (An et al., 2010). This discretization provides sufficient accuracy for values of the concentration parameter $b \leq 40$. Note, that $b \geq 20$ reflects a rather high degree of anisotropy for the fibers (Alastrué et al., 2009). Based on the symmetry properties of the ODF, 293 integration points, as referred to one half of the unit sphere, were used for the computations (see Figure 2 for the location of the integration points within the unit sphere). Note that this discretization takes also into account the contribution of myofibrils directed along the preferential direction $\mathbf{n}_0$. The set of directions and weights can be download at `http://web.maths.unsw.edu.au/~rsw/Sphere/EffSphDes/index.html`.

2.3. Particularization to One-dimension

Specification of the model to a one-dimensional case is helpful when performing the identification of the model parameters. In this case, the total

deviatoric strain energy function can be expressed as,

$$W^{1D}(\lambda) = W^{1D}_{matrix}(\lambda) + \rho_f \sum_i w^i \rho(\theta^i) W^{1D}_{mf}(\lambda, \lambda_r, \lambda^{w,r}_a, \lambda^{p,r}_a), \qquad (14)$$

where Eq. 12 has been used. The active part of the SEF now reads

$$W^{1D}_{mf,a}\left(\lambda, \lambda_r, \lambda^{w,r}_a, \lambda^{p,r}_a\right) = \frac{1}{2}\eta_1 A_1 \left[\ln\left(\lambda_r\right) - \ln\left(\lambda^{w,r}_a\right)\right]^2 + \\ + \frac{1}{2}\eta_2 A_2 \left[\ln\left(\lambda_r\right) - \ln\left(\lambda^{p,r}_a\right)\right]^2. \qquad (15)$$

Instead, for the passive behavior of the myofibrils, we assumed the following phenomenological SEF,

$$W^{1D}_{mf,p}\left(\lambda, \lambda_r\right) = C^f_{10}\left(\bar{I}_1 - 3\right) + C^f_{20}\left(\bar{I}_1 - 3\right)^2 + \frac{k^f_1}{2k^f_2}\left[e^{k^f_2\left\langle \bar{I}^r_4 - 1\right\rangle^2} - 1\right], \qquad (16)$$

where $\langle\circ\rangle = \frac{1}{2}\left(\circ + |\circ|\right)$, $\bar{I}_1 = \lambda^2 + \frac{2}{\lambda}$ and $\bar{I}^r_4 = \lambda^2_r$, while C^f_{10}, C^f_{20}, k^f_1 and k^f_2 are material constants assumed equal for all myofibrils and determined to best fit the stress-strain curves from the uniaxial test performed on single skeletal fibers reported by Rehorn et al. (2014). At last, the deviatoric strain energy function of the extracellular matrix is taken as,

$$W^{1D}_{matrix}\left(\lambda\right) = C^m_{10}\left(\bar{I}_1 - 3\right) + C^m_{30}\left(\bar{I}_1 - 3\right)^3, \qquad (17)$$

where C^m_{10} and C^m_{30} are the material constants obtained to best fitting the stress-strain curves from the uniaxial-test reported in Stefanati et al. (2020). In summary, for the single fiber, the one-dimensional SEF results,

$$W^{1D}(\lambda) = \sum_i w^i \rho(\theta^i) \left[W^{1D}_{mf,p}(\lambda, \lambda_i) + W^{1D}_{mf,a}(\lambda, \lambda_i, \lambda^{w,i}_a, \lambda^{p,i}_a)\right]. \qquad (18)$$

where $W^{1D}_{matrix}(\lambda) = 0$ and $\rho_f = 1$.

On the contrary, for the whole muscle is obtained

$$W^{1D}(\lambda) = W^{1D}_{matrix}(\lambda) + \rho_f \sum_i w^i \rho(\theta^i) \left[W^{1D}_{mf,p}(\lambda, \lambda_i) + W^{1D}_{mf,a}(\lambda, \lambda_i, \lambda_a^{w,i}, \lambda_a^{p,i}) \right]. \quad (19)$$

The first Piola-Kirchhoff stress tensor in the one-dimensional case is found as,

$$P = \frac{\partial W}{\partial \lambda}. \quad (20)$$

2.4. Characterization of the distribution function

The concentration parameter of the von Mises distribution, b, was identified as the best fit to the dispersion data reported in Schneidereit et al. (2018) in terms of the cosine angle of sum (CAS) defined as (Buttgereit et al., 2013)

$$\mathbf{CAS} = \frac{1}{4\pi} \int_{\mathbb{U}^2} \cos(\theta) \rho(\theta) dA = \sum_{i=1}^{m} \cos(\theta^i) w^i \rho(\theta^i). \quad (21)$$

In particular, b was determined using the average CAS value for the undeformed configuration, i.e. $\lambda = 1$ reported in Schneidereit et al. (2018) for healthy (CAS_{avg}=0.98) and dystrophic fibers (CAS_{avg}=0.89). In this regard, we found a value of $b = 3$ for the dystrophic fiber, and a value of $b = 20$ for the healthy fiber, consistent with a larger dispersion for the dystrophic fiber. The bottom panels in Figure 1b show a representation of the ODF for each case.

The model also allows computing changes in the myofibril alignment during concentric contraction. The modified CAS, CÂS, accounting for the

deformation of the fiber is easily computed as

$$\hat{\mathrm{CAS}} = \sum_{i=1}^{m} \left[\frac{(\mathbf{Fr}^i)}{\|\mathbf{Fr}^i\|} \cdot \mathbf{n}_0 \right] w^i \rho(\theta^i), \tag{22}$$

where $\left\|\mathbf{Fr}^i\right\|$ is the Euclidean norm.

2.5. Parameters identification of the model

The proposed framework can be used to model musculoskeletal tissue in general. However, since we were interested in studying mechanisms associated with DMD, the model has been specialized for healthy and dystrophic (mdx) mice. In particular, the attention has been placed on the diaphragm, which exhibits significant fibrosis as well as greatly impaired contractile function from an early age, and is regarded as a close phenotype to the human dystrophic muscle (Stedman and Sweeney, 1991).

Model parameters can be divided in three groups: i) cross-bridge kinetics parameters that regulate the myofilament kinetics and cross-bridge force generation (Table A.1), ii) structural parameters used for the definition of the filament overlap (Table A.1), and iii) mechanical parameters associated with the elasticity of passive and active elements (Table 1).

The structural parameters (except x_0) and the CSA fiber density (ρ_f) are the same reported in our previous work (Stefanati et al., 2020). On the contrary, the passive material parameters of the fiber (C_{10}^f, C_{20}^f, k_1^f, k_2^f) and the ECM (C_{10}^m, C_{30}^m) were identified again using the experimental data from Rehorn et al. (2014) in quasi-static condition for the fiber, and from Stefanati et al. (2020) for the ECM.

The remaining model parameters η_1, η_2, x_0 and the cross-bridges kinetics parameters (f_0, f_0', h, h', g, k_{on}^{Ca}, k_{off}^{Ca} shown in Table A.1) were found using

a constrained nonlinear fitting procedure described in Stefanati et al. (2020), and consisting in fitting normalized specific force-velocity curve for healthy and mdx mouse DIA (Coirault et al., 2003). Isometric stress for the healthy muscle and the concentric shortening velocity of both healthy and dystrophic muscle were constrained to be within the range reported in the literature. Due to the large variability in the reported isometric stress for the dystrophic muscle, this particular value was not included in the optimization process. However, it was verified the value predicted by the model to be within the experimental range. In addition, the cross-bridge kinetics parameters, the structural parameters, and the passive fiber response parameters were assumed equal for both the healthy and dystrophic muscle, since experimental observations support that the myosin function is not affected by dystrophy (Friedrich et al., 2010; Bates et al., 2013).

Table 1: Mechanical parameters of fiber and muscle in healthy and dystrophic muscle.

Parameters		fiber C57Bl	fiber MDX	Muscle C57Bl	Muscle MDX
b	(–)	20	3	20	3
η_1	(kPa)	0.1192×10^{-1}	0.3254×10^{-1}	0.1192×10^{-1}	0.3254×10^{-1}
η_2	(kPa)	7.1837×10^{-1}	7.1837×10^{-1}	7.1837×10^{-1}	7.1837×10^{-1}
C_{10}^f	(kPa)	9.8114	9.8114	9.8114	9.8114
C_{20}^f	(kPa)	5.3625	5.3625	5.3625	5.3625
k_1^f	(kPa)	2.7972×10^{-1}	2.7972×10^{-1}	2.7972×10^{-1}	2.7972×10^{-1}
k_2^f	(–)	2.3531×10^{-1}	2.3531×10^{-1}	2.3531×10^{-1}	2.3531×10^{-1}
C_{10}^m	(kPa)	×	×	2.5605	1.6886
C_{30}^m	(kPa)	×	×	1.1186×10^3	2.3130×10^3
ρ_f	(–)	×	×	1.0	0.8

The model and the optimization problem required for parameters model identification were implemented in MATLAB® version R2019a.

3. Results

This section summarizes the model's ability to reproduce the experimental data reported in the literature as well as its predicting capabilities. In this regard, model parameters associated with the passive response have been identified using stress-strain data at the fiber and muscle level. For the parameters associated with the active behavior, the isometric stress, the maximum concentric velocity, and the normalized concentric force-velocity curve at the muscle level were used. The performance of the identified model

was evaluated by comparing both the predicted eccentric force-velocity curve at the muscle level and the normalized concentric force-velocity curve at the fiber level with experimental data reported in the literature.

3.1. Concentric contraction

The optimization process has allowed reproducing the experimental data of maximum isometric force, maximum contraction velocity and the normalized concentric force-velocity curve for the healthy and dystrophic muscle reported in Coirault et al. (2003). The identified model parameters are found in Table 1 for the mechanical part and in Table A.1 for the myofilament kinetics and cross-bridge force generation, whereas Figure 3 shows the normalized specific force-velocity curve (F-V curve) obtained by the model using the parameters resulting from the fitting against the experimental curve reported in Coirault et al. (2003).

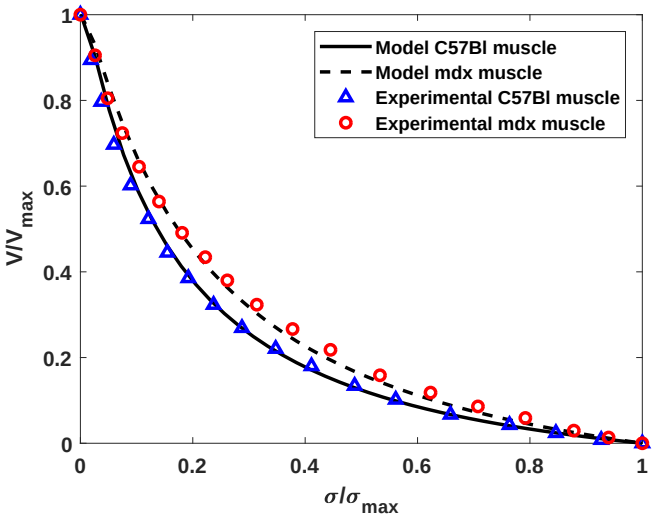

Figure 3: Normalized concentric specific force-velocity for C57Bl and mdx mouse diaphragm (Coirault et al., 2003), where σ is the total stress, σ_{max} is the isometric stress, V is $d\lambda/dt$ and V_{max} is the concentric velocity in unloaded conditions.

The fitting of the model is excellent as evidenced in the figure. Remarkably, the difference between healthy and dystrophic response is due to differences in the myofibril misalignment (different concentration parameter b) and in the value of parameter η_1, both parameters related to the ultrastructure of the underlying fibers. The maximum contraction velocity for the healthy and dystrophic muscles are within the experimental range, even though the percentage velocity reduction predicted by the model is slightly smaller as compared to the average value reported in the literature (see Table 2), but still within the experimental range. Regarding the dystrophic muscle, the model predicts isometric stress of 41.58 kPa, a 41% reduction with respect to the healthy case. This value corresponds to the average experimental value reported in the literature (Coirault et al., 1999; Bates et al., 2013).

Table 2: Simulations results of the mathematical model, where $\sigma_{\max}$ is the maximum isometric stress, $V_{\max} = \ln(\lambda_{\min})$ is the maximum shortening velocity in concentric contraction and $\varepsilon_{\min} = \ln(\lambda_{\min})$ is the maximum shortening strain in concentric contraction.

σ_{max} results for single fiber and DIA muscle

	$\sigma_{\max}$ (kPa)	$\sigma_{\max}$ (%) mdx vs C57Bl	Experiments (kPa) mean ± SD
fiber C57Bl	70.06	−25.81	68.7 ± 4.3 (Pellegrino et al., 2003)
fiber mdx	51.98		–
Muscle C57Bl	70.06	−40.65	67.69 ± 18.69 (Bates et al., 2013)
Muscle mdx	41.58		22.56 ± 1.70 (Bates et al., 2013)
			60.28 ± 35.40 (Coirault et al., 1999)

$V_{\max}$ results for single fiber and DIA muscle

	$V_{\max}$ (s^{-1})	$V_{\max}$ (%) mdx vs C57Bl	Experiments (s^{-1}) mean ± SD
fiber C57Bl	−7.95	−19.15	-6.59 ± 2.71 (Pellegrino et al., 2003)
fiber mdx	−6.43		–
Muscle C57Bl	−7.19	−17.18	-8.28 ± 1.09 (Coirault et al., 2003, 1999)
Muscle mdx	−5.96		-5.13 ± 0.99 (Coirault et al., 2003, 1999)

$\varepsilon_{\min}$ results for single fiber and DIA muscle

	$\lambda_{\min}$ (mm/mm)	$\varepsilon_{\min}$ (mm/mm)	$\varepsilon_{\min}$ (%) mdx vs C57Bl
Fiber C57Bl	0.6631	−0.4108	−19.84
Fiber mdx	0.7194	−0.3293	
Muscle C57Bl	0.8275	−0.1893	−22.55
Muscle mdx	0.8636	−0.1466	

Regarding tissue organization, the model predicts an increment in myofibrils misalignment during concentric contraction as shown in Figure 4. This behavior is in good agreement with the observations of Schneidereit et al. (2018) for both healthy and dystrophic fibers.

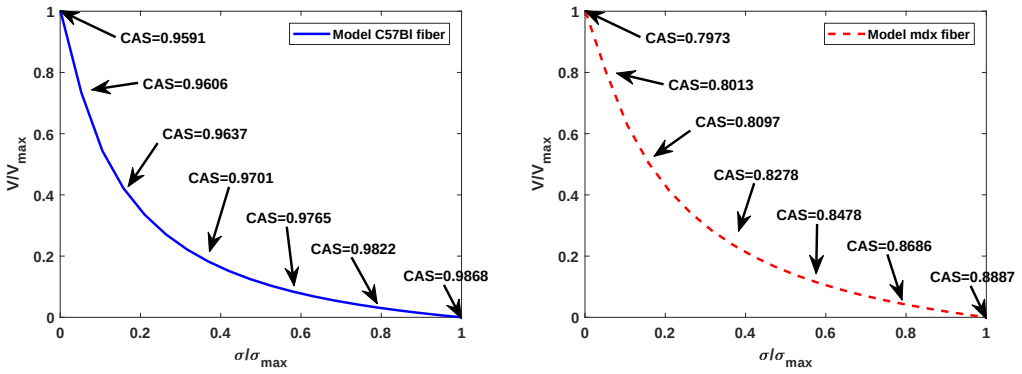

(a) (b)

Figure 4: a) Concentric F-V curve reporting CAS values at the maximum shortening stretch for fixed loads in healthy fiber. b) Concentric F-V curve reporting CAS values at the maximum shortening stretch for fixed loads in dystrophic fiber.

In Schneidereit et al. (2018), the CAS value is reported as a function of the single fiber stretch λ. Therefore, in order to perform a more quantitative comparison between model and experiments, we computed the CAS value for the range of contraction stretches reported in Schneidereit et al. (2018) with the result shown in Table 3. As shown in the table, the agreement with the experiments is excellent confirming the model's ability to reproduce the effects of increase myofibril disorganization during the active response of the muscle.

Table 3: Model CAS values obtained in the healthy and dystrophic fiber during concentric contraction for the range of contraction stretches reported in the literature. The experimental data of λ and CAS are taken from Schneidereit et al. (2018).

	Exp. λ (min – max)	Exp. CAS (min – max)	Model CAS (min – max)
Fiber C57Bl	0.729 – 1.0	0.951 – 0.996	0.968 – 0.987
Fiber mdx	0.857 – 1.0	0.844 – 0.951	0.851 – 0.889

3.2. Eccentric contraction and single fiber response

The capabilities of the model are further demonstrated in Figure 5 where the concentric-eccentric force-velocity curves predicted by the model for the healthy and dystrophic muscle, are compared against the experimental force-velocity curves reported in Till et al. (2008).

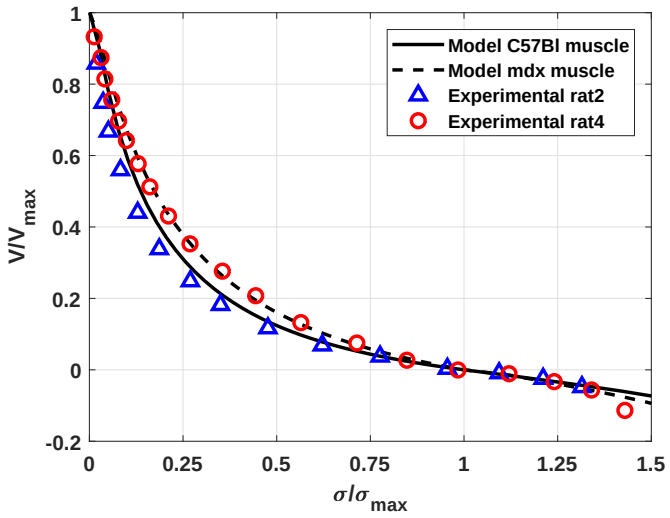

Figure 5: Normalized F-V curve for healthy and dystrophic muscle compared with experimental data of gastrocnemius medialis muscle (2 type fast fibers) of healthy adult male Wistar rats during concentric and eccentric contractions (Till et al., 2008). In eccentric condition (V/V_{max}<0), the muscle is stretched up to a fixed stretch of 1.04 (value in the range of experiments of Till et al. (2008)).

This example shows that the model is able to reproduce the concentric force-velocity curve for the rat, and predicts with reasonable accuracy the eccentric curve that has not been used for model parameters identification i.e., the eccentric response is predicted by the model.

Another important result is that the force-velocity curve predicted by the model for healthy and dystrophic fibers is in the range of the experiments for fast rat fibers (Type 2B) reported by Bottinelli et al. (1991) and fast mouse fiber (Type 2X and 2A) reported by Edman (2005), indicating the model predictive capabilities to reproduce the experimental data related to the isometric and concentric fiber contraction (see Figure 6). We also found excellent

agreement between the maximum isometric force and maximum contraction velocity in isolated fibers with the data reported in Pellegrino et al. (2003) (see Table 2).

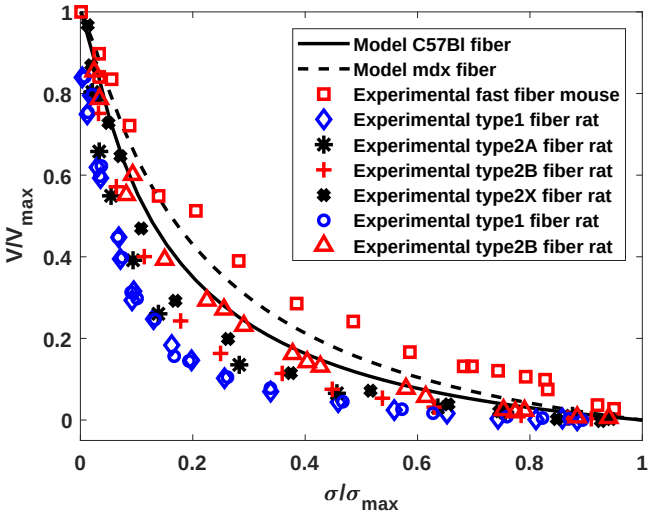

Figure 6: Normalized concentric F-V curve for healthy and dystrophic fiber compared with the experimental data for slow and fast healthy fiber (Bottinelli et al., 1991; Edman, 2005). Bottinelli et al. (1991) performed the experiments on single fibers from EDL, SOL and PL muscles of 3-month-old male Wistar rats, while (Edman, 2005) used single fibers from the flexor digitorum brevis muscle (FDB), where 2A and 2X fiber type were prevailing.

4. Discussion and conclusions

The implemented formulation of the model is able to reproduce the experimental data of maximum isometric stress and maximum contraction velocity for the healthy and dystrophic DIA, accounting for fibrosis and fat infiltration reported in the literature. In this regard, the maximum isometric stress predicted by the model for the dystrophic muscle is within the range

316 reported in the literature. The maximum contraction velocity predicted by
317 the model for the whole muscle was 7.19 and 5.96 1/s for healthy and dys-
318 trophic muscle respectively, within the range of 8.28 ± 1.09 and 5.13 ± 0.99
319 1/s reported in the literature (Coirault et al., 2003, 1999) for healthy and
320 dystrophic muscles, respectively.

321 Moreover, at the fiber level, the model provides for the dystrophic condi-
322 tion a 26% decrease of maximum isometric stress, a 19% decrease of maxi-
323 mum contraction velocity, and a 20% decrease of maximum shortening strain
324 than the healthy case. While, at the muscle scale, the model provides for
325 the dystrophic DIA a 41% decrease of maximum isometric stress, a 17% de-
326 crease of maximum contraction velocity, and a 23% decrease of maximum
327 shortening strain than the healthy muscle (see Table 2). These results are in
328 good agreement with the values reported in the literature (Bates et al., 2013;
329 Smith and Barton, 2014; Muller et al., 2001; Coirault et al., 2003, 1999), val-
330 idating the soundness of the proposed formulation.

331 Another important aspect of this work is that the model of the healthy
332 muscle is able to reproduce the eccentric F-V curve of rat gastrocnemius me-
333 dialis reported by Till et al. (2008). In addition, the concentric F-V curve
334 predicted by the model for the healthy and dystrophic fibers are within the
335 range of the experimental data (Bottinelli et al., 1991; Edman, 2005). This
336 result supports the model's ability to reproduce conditions not considered in
337 the process of parameters identification.

338 However, the most remarkable result is that the main difference in the ac-
339 tive behavior i.e., isometric stress and contraction velocity, between healthy
340 and dystrophic fibers is connected to the misalignment degree of the my-

ofibrils (ODF concentration parameter b) and the stiffness of the underlying myofibrils (parameter η_1). The value of b was found to be lower for the dystrophic fiber ($b = 3$) than for the healthy fiber ($b = 20$). This difference in b can be associated with alterations in the fiber microstructure, specifically in the myofibril alignment inside the single fiber, with a lower value of b indicating larger dispersion. This explanation is in agreement with the recent work of Schneidereit et al. (2018) in which they have studied the myofibrillar disorder in the single fiber of mdx EDL by means of second harmonic generation confocal microscopy. They measured the degree of local angular deviation of myofibrillar bundles from the main fiber axis (myofibrillar parallelism) finding significant myofibril disorganization in the dystrophic case with respect to the healthy case where highly aligned bundles were found. They also found a significant correlation between the loss of myofibrillar alignment and the reduction of contractile force in the mdx fiber, in line with the predictions of our model.

In addition, and more interestingly, the model demonstrates the high sensitivity of muscle performance to changes in its ultrastructure. More precisely, the results indicate that a variation of less than a 15% in the CAS between the healthy and the dystrophic fiber is able to account for a 41% reduction in the isometric force. This result is in agreement with what reported by Buttgereit et al. (2013) for the mdx mouse, and confirms the CAS may explain the progression of dystrophic fibers weakness that is related to alterations in the contractile apparatus geometry when compare to healthy muscle.

Myofibril misalignment also reduces the contraction velocity. However,

this effect on the contraction velocity is minor (less than 6%) as compared to the effect on the isometric force. On the contrary, contraction velocity was found to depend upon parameter η_1, associated with the stiffness of the underlying myofibril. In fact, η_1 was found to be about 2.5 times larger for the dystrophic myofibrils as compared to the healthy myofibrils. This difference in η_1 can be associated with the chaotic organization of the sarcomeres, in particular with the large VD of the dystrophic myofiber (Buttgereit et al., 2013). The Y-shaped structures defining the so-called "Verniers" are local deviations from perfectly alternating sarcomere patterns. Therefore, a larger VD implies a more chaotic structure of the sarcomere with a consequently less efficient filament sliding, and so, a lower fiber contraction.

Hence, the model suggests that at an early age, where myofibril misalignment is small (Buttgereit et al., 2013), the differences in the isometric force between dystrophic and healthy fibers should remain small, with this difference increasing with age as the degree of misalignment in the dystrophic fiber increases. On the contrary, differences in the contraction velocity between dystrophic and healthy fibers should be appreciable even at an early age since chaotic fibers are present at an early age (Buttgereit et al., 2013). In order to demonstrate these hypotheses, experiments characterizing the isometric force and contraction velocity with age, together with measurements of muscle microstructure i.e., CAS and VD, are required. These data will certainly provide a more clear picture of how alterations in myofibrillar alignment and sarcomeric order affect the mechanical performance of dystrophic muscle.

A limitation of the model is the lack of distinction between fast and slow contracting fibers that may otherwise help to reproduce more accurately the

shortening velocity at the muscle level as well as helping to identify additional mechanisms behind the loss of muscle functioning. Future investigations will also study the fiber-ECM interaction by looking into changes in the microstructure of the muscle during monoaxial loading when subjected to controlled mechanical deformation. These observations will allow us to formulate a much more accurate model of the tissue, as well as to determine potential mechanisms of damage that compromise muscular functioning in DMD.

In summary, a novel mathematical model for skeletal muscle is proposed. In particular, this model is an evolution of our previously developed model (Stefanati et al., 2020) including a specific characterization of the fiber ultrastructure, i.e. myofibrils alignment, sarcomere organization, and myofiber branching, in order to study how the changes in fiber ultrastructure affect the performance of the dystrophic skeletal muscle (in terms of isometric force and contraction velocity). In fact, differently to Stefanati et al. (2020) where the myofibrils are assumed to be perfectly aligned with the direction of the fiber, in the present model this condition is relaxed by allowing the myofibrils to be concentrated or dispersed with respect to the fiber direction, $\mathbf{n}_0$, according to a ODF, $\rho(\mathbf{r}, \mathbf{n}_0)$, assumed as a von Mises distribution.

In addition, the anisotropic model accounts for the organization of the myofibrils and is able to reproduce the skeletal muscle contraction for healthy and dystrophic case, showing excellent agreement with experimental data. Also, the model confirms the close correlation between the degradation in muscle performance (in terms of isometric force and contraction velocity) and alterations in the myofiber ultrastructure i.e., myofibril misalignment

and sarcomere organization. Last but not least, since the proposed formulation is invariant based, the presented model is amenable for implementation within a finite element framework (FEM), similar to the model reported in the literature by Hernández-Gascón et al. (2013). This resulting FEM model will allow studying muscle response on realistic geometries that will help to better understand the relationship between muscle pathology and the underlying muscle ultrastructure, and analyze how the effects of the micromechanical changes in the myofibrils propagate in the three-dimensional muscular district.

Acknowledgements

This work was also supported by a grant of the Association "Gli Amici di Emanuele Fondo DMD – Onlus".

Declaration of Competing Interest

The authors declare that they have no conflict of interest.

Appendix A.

In the Appendix A are reported, for completeness, the cross-bridges dynamics equations, and the remaining cross-bridge and structural parameters in a similar way as in Stefanati et al. (2020).

Variables

$Ca(t)$	Time course of free activator calcium available to myofilaments
$D(t)$	Time course of XBs in the detached state
$A_1(t)$	Time course of XBs in the attached, pre-power stroke A_1 state
$A_2(t)$	Time course of XBs in the attached, post-power stroke A_2 state

Structural Parameters

XB	Myosin cross-bridge
SL	Half sarcomere length
L_A	Length of thin filament
L_M	Length of thick filament
B	Bare zone on thick filament
Ov	Filament overlap zone allowing XB cycling
R_T	Total number of sites for XB attachment on half thick filament
R_{Ov}	Number of sites available for XB attachment within Ov
x_0	Average distortion of XB induced by power stroke
L_0	Chosen initial half-sarcomere length
A_s	Cross section area of a representative sarcomere

Kinetic Parameters

Ca_{50}	Calcium concentration of half saturation of RU
k_{on}^{0}	Rate coefficient regulating switching on of RU when no calcium is bound
k_{on}^{Ca}	Rate coefficient regulating switching on of RU when calcium is bound
k_{off}^{0}	Rate coefficient regulating switching off of RU when no calcium is bound
k_{off}^{Ca}	Rate coefficient regulating switching off of RU when calcium is bound
f	Rate coefficient regulating forward XB attachment step
f'	Rate coefficient regulating backward XB attachment step
h	Rate coefficient regulating forward XB power stroke
h'	Rate coefficient regulating backward XB power stroke
g	Rate coefficient regulating forward XB detachment step
u	Parameter grading strength of RU-RU nearest neighbor interaction
w	Parameter grading strength of XB-RU nearest neighbor interaction
v	Parameter grading strength of XB-XB nearest neighbor interaction

Activator Calcium Dependence.

$$k_{on}^{ref} = k_{on}^{0} + (k_{on}^{Ca} - k_{on}^{0}) \cdot \frac{Ca(t)}{Ca(t) + Ca_{50}}, \tag{A.1}$$

$$k_{off}^{ref} = k_{off}^{0} + (k_{off}^{Ca} - k_{off}^{0}) \cdot \frac{Ca(t)}{Ca(t) + Ca_{50}}. \tag{A.2}$$

Sarcomere Length Dependence: Filament Overlap (Linear function).

$$Ov(\lambda) = \begin{cases} \frac{1}{2} \cdot [L_M + 2 \cdot SL] - L_A & \text{if } 2 \cdot SL < 2 \cdot L_A - B, \\ \frac{1}{2} \cdot [L_M - B] & \text{if } 2 \cdot L_A - B \leq 2 \cdot SL < 2 \cdot L_A + B, \\ \frac{1}{2} \cdot [L_M - 2 \cdot SL] + L_A & \text{if } 2 \cdot SL \geq 2 \cdot L_A + B. \end{cases} \tag{A.3}$$

$$R_{Ov}(t) = \frac{Ov}{\frac{1}{2} \cdot (L_M - B)} \cdot R_T, \qquad R_{off}(t) = R_{Ov}(t) - D(t) - A_1(t) - A_2(t). \tag{A.4}$$

State Variable-Dependent Coefficients: Neighbor Interactions (RU-RU, XB-RU and XB-XB). Since the values of u, w and v are chosen equal to 1,

$$k_{on} = k_{on}^{ref}, \quad k_{off} = k_{off}^{ref}, \quad f = f_0, \quad f' = f_0. \tag{A.5}$$

Cross-bridge kinetics.

$$\frac{dD(t)}{dt} = k_{on} \cdot R_{off}(t) + f' \cdot A_1(t) + g \cdot A_2(t) - \Big[k_{off} + f\Big] \cdot D(t), \tag{A.6}$$

$$\frac{dA_1(t)}{dt} = f \cdot D(t) + h' \cdot A_2(t) - \Big[f' + h\Big] \cdot A_1(t), \tag{A.7}$$

$$\frac{dA_2(t)}{dt} = h \cdot A_1(t) - \Big[h' + g\Big] \cdot A_2(t). \tag{A.8}$$

Distortion imposed by shear motion between thick and thin filaments in both the A_1 weak and A_2 power stroke states. The values of $x_s^{w,r} = 0.0004$ and $x_s^{p,r} = 0.0244$ are the cross-bridge deformation in steady state conditions, while $\lambda_r = \sqrt{\mathbf{r} \cdot (\bar{\mathbf{C}} \cdot \mathbf{r})}$ is the isochoric stretch in the myofibril direction.

$$\begin{aligned} \frac{ds_1(t)}{dt} &= \left(f \cdot \frac{D(t)}{A_1(t)} + h' \cdot \frac{A_2(t)}{A_1(t)}\right) \cdot \Big[\ln\big(\lambda_r\big) - s_1(t) - x_s^{w,r}\Big], \\ \frac{ds_2(t)}{dt} &= h \cdot \frac{A_1(t)}{A_2(t)} \cdot \Big[\ln\big(\lambda_r\big) - s_2(t) - x_s^{p,r}\Big]. \end{aligned} \tag{A.9}$$

Table A.1 shows the cross-bridge kinetics and structural parameters.

Table A.1: Parameters of the mathematical model.

Cross-bridge kinetics parameters

f_0 (s^{-1})	f_0' (s^{-1})	h (s^{-1})	h' (s^{-1})	g (s^{-1})
93.2707	841.9648	15.6093	10.9897	27.5246
k_{on}^{Ca} (s^{-1})	k_{off}^{Ca} (s^{-1})	k_{on}^{0} (s^{-1})	k_{off}^{0} (s^{-1})	Ca_{50} (ML^{-1})
181.5351	99.9861	0.0	198.0158	1.78×10^{-6}

Structural parameters

L_A (μm)	B (μm)	L_M (μm)	L_0 (μm)
1.2	0.2	1.6	1.1
x_0 (μm)	R_T (adim.)	A_s (mm^2)	$f(Ca)$
0.0268	1.62×10^5	3×10^{-6}	0.9825

Acharyya, S., Villalta, S., Bakkar, N., Bupha-Intr, T., Janssen, P., Carathers, M., Li, Z., Beg, A., Ghosh, S., Sahenk, Z., Weinstein, M., Gardner, K., Rafael-Fortney, J., Karin, M., Tidball, J., Baldwin, A., Guttridge, D., 2007. Interplay of ikk/nf-κb signaling in macrophages and myofibers promotes muscle degeneration in duchenne muscular dystrophy. The Journal of Clinical Investigation 117, 889–901.

Alastrué, V., Martinez, M.A., Doblaré, M., Menzel, A., 2009. Anisotropic micro-sphere-based finite elasticity applied to blood vessel modelling. Journal of the Mechanics and Physics of Solids 57, 178–203.

444 An, C., Chen, X., Sloan, I.H., Womersley, R.S., 2010. Well conditioned
445 spherical designs for integration and interpolation on the two-sphere. SIAM
446 journal on numerical analysis 48, 2135–2157.

447 Bates, G., Sigurdardottir, S., Kachmar, L., Zitouni, N., Benedetti, A., Petrof,
448 B., Rassier, D., Lauzon, A., 2013. Molecular, cellular, and muscle strip
449 mechanics of the mdx mouse diaphragm. American Journal of Physiology
450 - Cell Physiology 304, C873–C880.

451 Bottinelli, R., Schiaffino, S., Reggiani, C., 1991. Force-velocity relations and
452 myosin heavy chain isoform compositions of skinned fibres from rat skeletal
453 muscle. The Journal of Physiology 437, 655–672.

454 Buttgereit, A., Weber, C., Garbe, C., Friedrich, O., 2013. From chaos to
455 split-ups - SHG microscopy reveals a specific remodelling mechanism in
456 ageing dystrophic muscle. The Journal of Pathology 229, 477–485.

457 Coirault, C., Lambert, F., Marchand-Adam, S., Attal, P., Chemla, D., Lecar-
458 pentier, Y., 1999. Myosin molecular motor dysfunction in dystrophic mouse
459 diaphragm. American Journal of Physiology - Cell Physiology 277, C1170–
460 C1176.

461 Coirault, C., Pignol, B., Cooper, R., Butler-Browne, G., Chabrier, P., Lecar-
462 pentier, Y., 2003. Severe muscle dysfunction precedes collagen tissue pro-
463 liferation in mdx mouse diaphragm. Journal of Applied Physiology 94,
464 1744–1750.

465 Edman, K., 2005. Contractile properties of mouse single muscle fibers, a

comparison with amphibian muscle fibers. Journal of Experimental Biology 208, 1905–1913.

Friedrich, O., Both, M., Weber, C., Schürmann, S., Teichmann, M.D.H., Von Wegner, F., Fink, R.H.A., Vogel, M., Chamberlain, J.S., Garbe, C., 2010. Microarchitecture is severely compromised but motor protein function is preserved in dystrophic mdx skeletal muscle. Biophysical Journal 98, 606–616.

Friedrich, O., von Wegner, F., Chamberlain, J., Fink, R., Rohrbach, P., 2008. L-Type Ca^{2+} Channel Function Is Linked to Dystrophin Expression in Mammalian Muscle. PLoS ONE 3, 1–12.

Garbe, C., Buttgereit, A., Schurmann, S., Friedrich, O., 2012. Automated multiscale morphometry of muscle disease from second harmonic generation microscopy using tensor-based image processing. IEEE Transactions on Biomedical Engineering 59, 39–44.

Gasser, T., Ogden, R., Holzapfel, G., 2006. Hyperelastic modelling of arterial layers with distributed collagen fibre orientations. Journal of the Royal Society Interface 3, 15–35.

Head, S., Williams, D., Stephenson, D., Gage, P., 1992. Abnormalities in structure and function of limb skeletal muscle fibres of dystrophic *mdx* mice. Proceedings of the Royal Society of London. Series B: Biological Sciences 248, 163–169.

Heidlauf, T., Röhrle, O., 2014. A multiscale chemo-electro-mechanical skele-

tal muscle model to analyze muscle contraction and force generation for different muscle fiber arrangements. Frontiers in Physiology 5, 1–14.

Hernández-Gascón, B., Grasa, J., Calvo, B., Rodríguez, J., 2013. A 3d electro-mechanical continuum model for simulating skeletal muscle contraction. Journal of Theoretical Biology 335, 108–118.

Karami, M., Calvo, B., Zohoor, H., Firoozbakhsh, K., Grasa, J., 2019. Assessing the role of Ca^{2+} in skeletal muscle fatigue using a multi-scale continuum model. Journal of Theoretical Biology 461, 76 – 83.

Messina, S., Altavilla, D., Aguennouz, M., Seminara, P., Minutoli, L., Monici, M., Bitto, A., Mazzeo, A., Marini, H., Squadrito, F., 2006. Lipid peroxidation inhibition blunts nuclear factor-κb activation, reduces skeletal muscle degeneration, and enhances muscle function in mdx mice. The American Journal of Pathology 168, 918–926.

Muller, J., Vayssiere, N., Royuela, M., Leger, M., Muller, A., Bacou, F., Pons, F., Hugon, G., Mornet, D., 2001. Comparative evolution of muscular dystrophy in diaphragm, gastrocnemius and masseter muscles from old male mdx mice. Journal of Muscle Research and Cell Motility 22, 133–139.

Pellegrino, M.A., Canepari, M., Rossi, R., D'Antona, G., Reggiani, C., Bottinelli, R., 2003. Orthologous myosin isoforms and scaling of shortening velocity with body size in mouse, rat, rabbit and human muscles. The Journal of Physiology 546, 677–689.

Petrof, B., Shrager, J., Stedman, H., Kelly, A., Sweeney, H., 1993. Dystrophin protects the sarcolemma from stresses developed during muscle contraction. Proceedings of the National Academy of Sciences of the United States of America 90, 3710–3714.

Rehorn, M.R., Schroer, A.K., Blemker, S.S., 2014. The passive properties of muscle fibers are velocity dependent. Journal of biomechanics 47, 687–693.

Schneidereit, D., Nübler, S., Prölß, G., Reischl, B., Schürmann, S., Müller, O., Friedrich, O., 2018. Optical prediction of single muscle fiber force production using a combined biomechatronics and second harmonic generation imaging approach. Light: Science & Applications 7:79, 1–14.

Smith, L., Barton, E., 2014. Collagen content does not alter the passive mechanical properties of fibrotic skeletal muscle in mdx mice. American Journal of Physiology - Cell Physiology 306, C889–C898.

Stedman, H., Sweeney, H., 1991. The mdx mouse diaphragm reproduces the degenerative changes of duchenne muscular dystrophy. Nature 352, 536–539.

Stefanati, M., Villa, C., Torrente, Y., Rodriguez Matas, J., 2020. A mathematical model of healthy and dystrophic skeletal muscle biomechanics. Journal of the Mechanics and Physics of Solids 134, 1–16.

Till, O., Siebert, T., Rode, C., Blickhan, R., 2008. Characterization of isovelocity extension of activated muscle: a hill-type model for eccentric contractions and a method for parameter determination. Journal of Theoretical Biology 255, 176–187.